

REPORT DOCUMENTATION PAGE			Form Approved OMB No. 0704-0188	
<small>Public reporting burden for this collection of information is estimated to average 1 hour per response, including the time for reviewing instructions, searching existing data sources, gathering and maintaining the data needed, and completing and reviewing this collection of information. Send comments regarding this burden estimate or any other aspect of this collection of information, including suggestions for reducing this burden to Department of Defense, Washington Headquarters Services, Directorate for Information Operations and Reports (0704-0188), 1215 Jefferson Davis Highway, Suite 1204, Arlington, VA 22202-4302. Respondents should be aware that notwithstanding any other provision of law, no person shall be subject to any penalty for failing to comply with a collection of information if it does not display a currently valid OMB control number. PLEASE DO NOT RETURN YOUR FORM TO THE ABOVE ADDRESS.</small>				
1. REPORT DATE (DD-MM-YYYY) 11-06-2007		2. REPORT TYPE Final Technical Report		3. DATES COVERED (From - To) 01-01-2004 to 31-12-2006
4. TITLE AND SUBTITLE  Charged Particle Ejection from Nanolayered Heterostructures			5a. CONTRACT NUMBER	
			5b. GRANT NUMBER FA9550-04-1-0004	
			5c. PROGRAM ELEMENT NUMBER	
6. AUTHOR(S)  Dennis C. Jacobs			5d. PROJECT NUMBER	
			5e. TASK NUMBER	
			5f. WORK UNIT NUMBER	
7. PERFORMING ORGANIZATION NAME(S) AND ADDRESS(ES)  University of Notre Dame 511 Main Building Notre Dame, IN 46556			8. PERFORMING ORGANIZATION REPORT	
9. SPONSORING / MONITORING AGENCY NAME(S) AND ADDRESS(ES)  Attn: Dr. Michael R. Berman AFOSR/NA 875 N. Randolph St. Suite 325, Room 3112 Arlington, VA 22203			10. SPONSOR/MONITOR'S ACRONYM(S) AFOSR/NA	
12. DISTRIBUTION / AVAILABILITY STATEMENT  Approved for public release, distribution unlimited.			AFRL-SR-AR-TR-07-0206	
13. SUPPLEMENTARY NOTES The views, opinions and/or findings contained in this report are those of the author and should not be construed as an official Air Force position, policy, or decision.				
14. ABSTRACT  This project explored specific strategies to augment the plasma density surrounding hypersonic vehicles through novel Metal-Insulator-Metal (MIM) nanostructures. Solid-state devices based on the MIM architecture emit hot electrons when a voltage bias is applied across the metal electrodes. The performance of a variety of MIM devices was studied as a function of the fabrication characteristics. The energy distribution of the emitted electrons was acquired to gain insight into the hot electron transport mechanism within these unique devices.				
15. SUBJECT TERMS Deposition, Thin-films, Nanofabrication				
16. SECURITY CLASSIFICATION OF: Unclassified			17. LIMITATION OF ABSTRACT  UL	18. NUMBER OF PAGES  36
a. REPORT Unclassified	b. ABSTRACT Unclassified	c. THIS PAGE Unclassified	19a. NAME OF RESPONSIBLE PERSON Dennis C. Jacobs	
			19b. TELEPHONE NUMBER (include area code) (574) 631-8023	

UNIVERSITY OF  
NOTRE DAME

Department of Chemistry and Biochemistry  
University of Notre Dame  
Notre Dame, IN 46556

---

Air Force Office of Scientific Research  
Plasma Dynamics for Aerospace Applications Theme  
Grant # FA9550-04-1-0004  
Final Technical Report  
1 January 2004 – 31 December 2006

**Charged Particle Ejection from  
Nanolayered Heterostructures**

Dennis C. Jacobs, Ph.D.  
*Principal Investigator*

---

Approved for public release; distribution is unlimited.

---

## Table of Contents

<b>1. Research Objectives .....</b>	<b>4</b>
<b>2. Experimental Approach .....</b>	<b>5</b>
2.1. Fabrication of thin-film cold cathode devices .....	5
2.2. Testing of thin-film cold cathode devices .....	6
<b>3. Results and Discussion .....</b>	<b>7</b>
3.1. Combinatorial screening of device fabrication parameters and effects on cold cathode performance- Ti/SiO <sub>x</sub> /Au .....	7
3.1.1. Variation of layer thickness for the top metal electrode (Au) .....	7
3.1.2. Variation of layer thickness for the insulator (SiO <sub>x</sub> ) .....	9
3.1.3. Variation of pressure of 20% Oxygen/Argon pressure for reactive evaporation of the insulator (SiO <sub>x</sub> ) .....	12
3.2. Improvements in cold cathode performance and characterization scheme ...	14
3.3. Characterization of cold cathode performance for Ti/Au/SiO <sub>x</sub> /Au devices ...	16
3.3.1. Voltage ramp cycles for device current measurement- Ti/Au/SiO <sub>x</sub> /Au ...	16
3.3.2. Effect of temperature on device current- Ti/Au/SiO <sub>x</sub> /Au .....	19
3.3.3. Electron energy distributions- Ti/Au/SiO <sub>x</sub> /Au .....	19
3.3.4. Relaxation effects in device and emission currents- Ti/Au/SiO <sub>x</sub> /Au .....	21
3.3.5. Lifetime test for emission current- Ti/Au/SiO <sub>x</sub> /Au .....	22
3.3.6. Emission current-Normalized energy distributions at series of voltage biases- Ti/Au/SiO <sub>x</sub> /Au .....	22
3.3.7. Transmission efficiency of hemispherical energy analyzer- Ti/Au/SiO <sub>x</sub> /Au .....	25
3.3.8. Transmission corrected normalized distributions- Ti/Au/SiO <sub>x</sub> /Au .....	26
3.4. Discussion .....	28
<b>4. Summary .....</b>	<b>32</b>
<b>5. References .....</b>	<b>33</b>
<b>6. Personnel Supported .....</b>	<b>36</b>
<b>7. Publications .....</b>	<b>36</b>
<b>8. Interactions/Transitions .....</b>	<b>36</b>
<b>9. Inventions or Patent Disclosures .....</b>	<b>36</b>
<b>10. Honors and Awards .....</b>	<b>36</b>



## 1. Research Objectives

The development of many advanced technologies for aerospace applications (e.g., drag reduction, electromagnetic cloaking, combustion enhancement, and magneto gas dynamic control) relies on a weakly ionized plasma flow around the vehicle.<sup>1</sup> To help realize this goal, experiments were performed to develop a novel solid-state device capable of providing cold-cathode electron ejection. The Metal-Insulator-Metal (MIM) heterostructure delivers ballistic hot electrons to the surface from the solid side of the gas/surface interface.<sup>2</sup> Encasing the surface of a hypersonic vehicle with functioning MIM devices could increase the electron density in the boundary layer surrounding the vehicle.

The basic design of the M-I-M device is shown in Figure 1. When the metal overlayer is biased positive relative to the metal underlayer, electron transport through the insulating layer occurs. The objectives of this research grant were to fabricate operational MIM devices and to measure the efficiency and kinetic energy distribution of electrons emitted from the device.

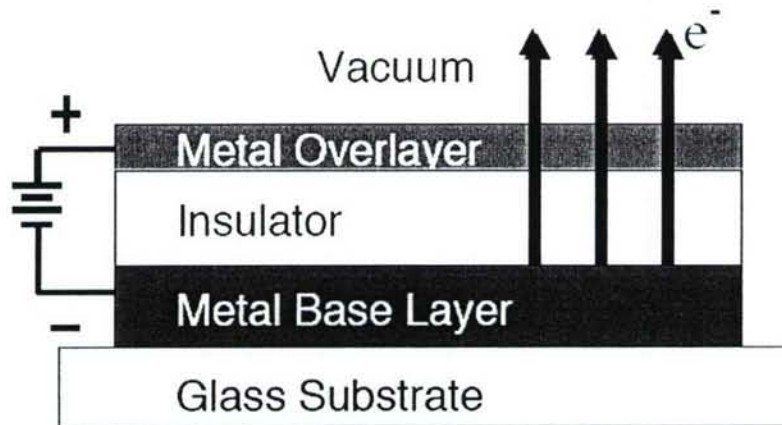


Figure 1. Schematic diagram for a biased MIM cold cathode device

## 2. Experimental Approach

### 2.1. Fabrication of thin-film cold cathode devices

Thin-film cold cathode devices based on Metal-Insulator-Metal (MIM) architecture were fabricated by electron beam evaporation. The thickness of each deposited layer was monitored by a quartz crystal microbalance during fabrication, and a combinatorial approach was employed to screen for the optimal thickness and composition for each layer. The total thickness of the device ranged between 75-100 nm. In two different sets of experiments, devices were fabricated by using different masks to pattern the devices on a glass substrate. The pre-patterned glass substrate has 10 gold electrodes that facilitate the electrical testing of fabricated devices by depositing the stripes of metal layers of the device such that they overlap with 2 gold electrodes on the pre-patterned glass substrate. The design of the pre-patterned glass substrate allows fabrication of a maximum of 24 devices. Although initial screening was done by fabricating an array of 24 devices in each experiment, it was found necessary to fabricate 12 devices for acquisition of electron energy distributions. An array of 12 devices was fabricated in order to mitigate the possible effect on the trajectories of vacuum-emitted electrons due to electric fields in the vicinity of the tested device. The electric fields are imposed due to the voltages on the top electrodes of the devices in the array. In the first set of experiments, 12 devices, composed of Ti/SiO<sub>x</sub>/Au (Gold top electrode), were fabricated and screened for optimal layer thicknesses and fabrication conditions to maximize cold cathode emission. In the second set of experiments, only three devices were patterned on the glass substrate by employing a series of masks during fabrication, and devices composed of Ti/Au/SiO<sub>x</sub>/Au (Gold top electrode) were tested for emission. The second set of experiments provided accurate device currents since the design of the mask for the second set of experiments eliminated the detrimental effect of thinning of the deposited oxide layer at the edges of the insulator mask. Since the Gold/Insulator interface for the bottom metal electrode was found to enhance the total emission current for the cold cathode compared to Titanium/Insulator interface, the composition of the bottom metal electrode was changed for the second set of experiments to achieve enhanced emission. The insulator layer in the MIM device was comprised of TiO<sub>2</sub>, Al<sub>2</sub>O<sub>3</sub> or SiO<sub>2</sub>- all deposited by reactive evaporation. Devices composed of TiO<sub>x</sub> layer sandwiched between the metal electrodes did not show cold cathode emission, while emission current from devices composed of Al<sub>2</sub>O<sub>3</sub> insulator layer showed similar performance to that of devices with SiO<sub>x</sub> as the insulator layer. The optimization of the fabrication procedure was carried out for devices with SiO<sub>x</sub> as the insulator layer.

The first step in the fabrication procedure consists of cleaning the glass substrate by sonication in Ethanol and blow drying in dry Nitrogen before introducing the substrate into the vacuum chamber. The pre-patterned glass substrate has 10 gold electrodes, and each device is tested for emission by applying a voltage bias between a pair of Gold electrodes. The substrate is heated to 250-300 Celsius for about 1 hour, and the crucibles for the materials are outgassed sequentially during that time to get rid of any volatile contaminants. The bottom electrode of the MIM device consists of either, a layer of Titanium (35 nm) in the first set of experiments, or a wetting layer of Titanium (5 nm)



stacked by a Gold layer (30 nm) in the second set of experiments. In both sets of experiments, only the titanium layer in the bottom metal electrode is deposited at the elevated temperature. Subsequent to deposition of Titanium layer in the bottom metal electrode, the substrate is cooled to room temperature before continuing with the deposition of other layers in the device. The insulator layer in the devices was silicon dioxide and was evaporated in a background pressure of  $1 \times 10^{-6}$  Torr or  $8 \times 10^{-6}$  of 20% Oxygen/Argon mixture. The typical base pressure of the chamber without the Oxygen/Argon mixture was  $3-4 \times 10^{-7}$  Torr. The thickness of the insulator layer ranged between 20-40 nm while the thickness for the top Gold electrode was varied between 15-25 nm.

## **2.2. Testing of thin-film cold cathode devices**

The performance of the fabricated cold cathode devices was evaluated by recording the total emission current, energy distributions for the emitted electrons, and the device current between the metal electrodes. All observables were recorded as a function of the applied voltage bias between the metal electrodes. The tests also consisted of monitoring the total emission current at a constant voltage bias as a function of time to determine the longevity of the emission.

In the first set of experiments, Ti/SiO<sub>x</sub>/Au MIM devices were studied to determine the optimal fabrication procedure to maximize cold cathode emission. The selection of voltage bias applied across the metal electrodes of each device was such that when a device is being tested for emission, the other devices are either reverse biased, or forward biased around 5V where vacuum emission is not expected, or zero voltage bias is applied between the metal electrodes of the device. This scheme ensures that only emission from the device under test is recorded. Each of the 12 MIM devices fabricated on the glass substrate was cycled through 25 voltage ramp cycles between 4-12 V. The 25 voltage ramp cycles were grouped in 5 rounds, and each round of testing consisted of 5 consecutive voltage ramp cycles. The 5 rounds of voltage ramp cycles on each of the 12 devices were performed in a random order. This strategy ensures that each of the devices will sample a random bias history, and the identification of the optimal fabrication procedure will not be influenced by effects of a particular sequence of voltage bias history. In order to quantify the performance of vacuum emission from the cold cathode devices, the total emission current readings at voltage bias of 12 V in the voltage ramp cycles is compared as the fabrication conditions, including layer thicknesses and oxygen/argon pressure for reactive evaporation, are varied. Each array of 12 devices is fabricated at a chosen composition, and the total data set for the array consisting of  $25 \times 12$  readings is binned both, by total emission current, and by time elapsed since turning on the voltages to test the array of devices. This testing routine and assessment scheme helps in identifying MIM device composition that is favorable for both, maximizing the emission current, and the longevity of the devices.

Preliminary results suggested that normalization of the electron energy distributions to the total emission current during acquisition of the distribution will be a

good strategy to correct for fluctuations and variation of emission current with time. The normalization routine consisted of dividing the counts at a given electron energy in the scan (recorded by the hemispherical energy analyzer) by the average total emission current collected at the first ion-optics element of an entrance einzel lens during the same time interval. The first ion-optic element of the entrance einzel lens is connected to ground potential through a Keithley electrometer to monitor the emission current during the scan.

The hemispherical energy analyzer has an energy dependent transmission efficiency that attenuates detection of the low energy electrons. Two strategies were employed to minimize and correct for the filtering of the low energy electrons. In the first strategy, the top metal electrode of the MIM device was held at a constant voltage of -4.8 V. The additional kinetic energy imparted to the emitted electrons from the MIM device should improve the sensitivity to low energy electrons. In the second strategy, the transmission efficiency of the detector was determined by recording emission current-normalized electron energy distributions at a constant voltage bias of 12V across the MIM device, but at different voltages for the top metal electrode. The transmission efficiency was determined by plotting the normalized counts at the peak of the distribution versus the electron energy at the peak in the distribution. The functional fit for the empirically determined transmission efficiency was used to correct the energy distributions. Additionally, a series of electron energy distributions at different voltage biases across the MIM device were also recorded at an increased top electrode voltage of -6.5 V to reduce the magnitude of corrections to the distributions.

### **3. Results and Discussion**

#### **3.1. Combinatorial screening of device fabrication parameters and effects on cold cathode performance- Ti/SiO<sub>x</sub>/Au**

##### **3.1.1. Variation of layer thickness for the top metal electrode (Au)**

The emission current readings are binned by the magnitude of emission currents in consecutive time bins, and each time bin is approximately 3 hours in duration. This scheme presents both, the fractional distribution of emission current magnitudes in each time bin, and allows easy comparison of performance of cold cathode emission between different time bins. The thickness of the top metal electrode was varied between 20-30 nm in the fabrication procedure, while in each case the SiO<sub>2</sub> insulator layer was deposited in a background of 20% Oxygen/Argon atmosphere at a base pressure of  $1 \times 10^{-6}$  Torr. The histograms for the different layer thicknesses are presented in fig. 2.

The histograms plotted for each layer thickness show that the emission current magnitudes cluster in two regimes- one below 100 pA and the other between 1000-5000 pA. For the 20 nm electrode thickness, a large fraction of the emission current readings are below 100 pA for all the time bins, with the exception for time bins greater



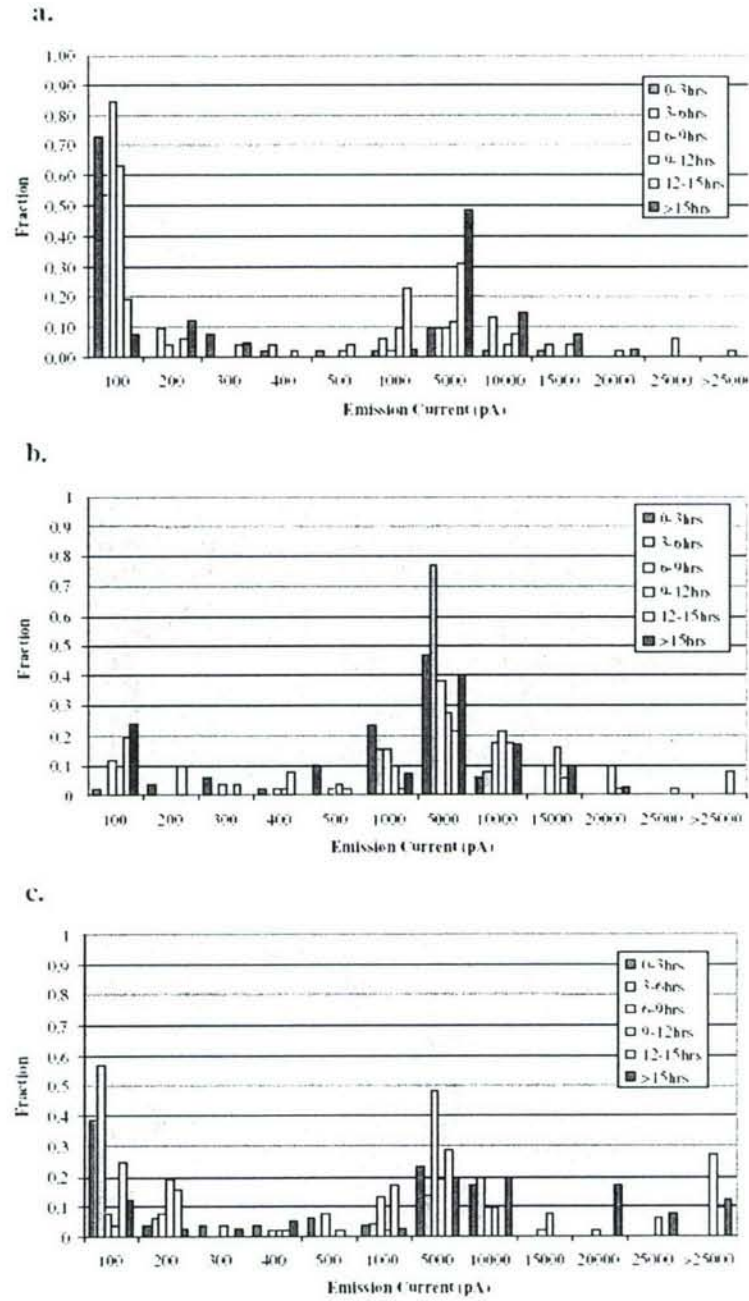


**Figure 2. Emission current histograms for readings at 12V bias in the voltage ramp cycles at different top electrode thicknesses- a. 20 nm, b. 25 nm, and c. 30 nm.**



than 12 hours where 30% and 50% of the readings respectively for time bins in incremental order are in the 5000 pA emission current bin. In contrast to the results for the 20 nm electrode thickness, the histograms for the emission current readings for both 25 nm and 30 nm top electrode thicknesses show emission at currents of 1000-5000 pA even in the early time bins. Comparing the performance of devices with top electrode thicknesses of 25 nm and 30 nm reveals that in the former case the emission current bin between 1000-5000 pA is populated by a larger fraction of the emission current readings than the same for the latter case for majority of the time bins. The performance of cold cathode emission for the different top electrode thicknesses is quantified in table 1 by calculating the fractions for emission current below 500 pA and above 1000 pA after 10 hours of testing. A comparison between data tabulated for different top electrode thicknesses indicates that devices with a top metal electrode thickness of 25 nm perform optimally in terms of magnitude and longevity of the emission current.

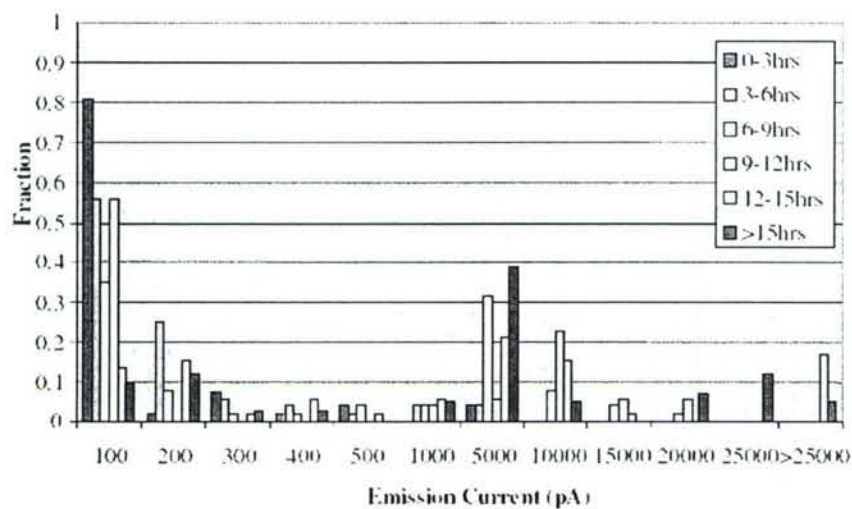
**Table 1**  
**Performance of cold cathode emission after 10 hours of testing - variation of top electrode thickness**

Thickness (nm)	Total fraction below 500 pA	Total fraction above 1000 pA
20	0.39	0.47
25 (#1)	0.26	0.70
30	0.35	0.56
25 (#2)	0.34	0.64

### 3.1.2. Variation of layer thickness for the insulator ( $\text{SiO}_x$ )

Histograms for emission current readings were binned by emission current and time for devices fabricated with different insulator thicknesses ranging between 20-40 nm. The  $\text{SiO}_2$  insulator layer was deposited in a 20% Oxygen/Argon environment at a base pressure of  $1 \times 10^{-6}$  Torr, and the thickness of the top metal electrode was 25 nm in each case. Figure 3 shows the histograms for cold cathode emission data for different thicknesses of the insulator layer. At an insulator thickness of 40 nm, the emission current is predominantly below 100 pA even after testing for over 15 hours. For insulator thicknesses less than 40 nm, the fractional distribution of emission current peaks below 100 pA and 1000-5000 pA range. The fractional distribution for insulator thickness of 20 nm shows that greater than 50% of the readings are below 100 pA for the first 6 hours of testing. Only after testing the devices for over 6 hours, the 5000 pA bin for emission current is populated over 30% for the first time in the test. In contrast to the observations for the 20 nm thickness, emission currents between 1000-5000 pA are observed in the early time bins for 25 and 30 nm insulator thicknesses. The distributions for the 25 nm and 30 nm thicknesses are similar with approximately 45% and 20% of readings in the respective cases observed in the 1000-5000 pA range in the first time bin of 0-3 hours. A comparison of the distributions for the 25 and 30 nm thicknesses in the early time bins

a.



b.

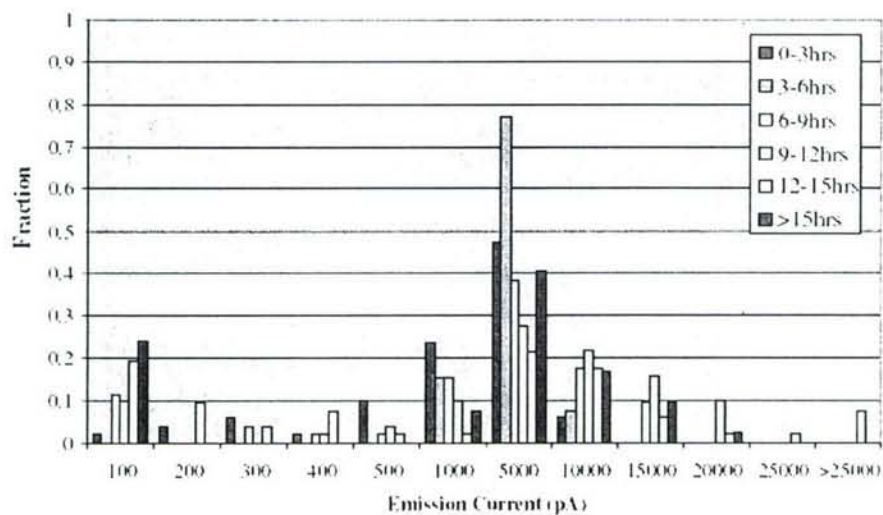
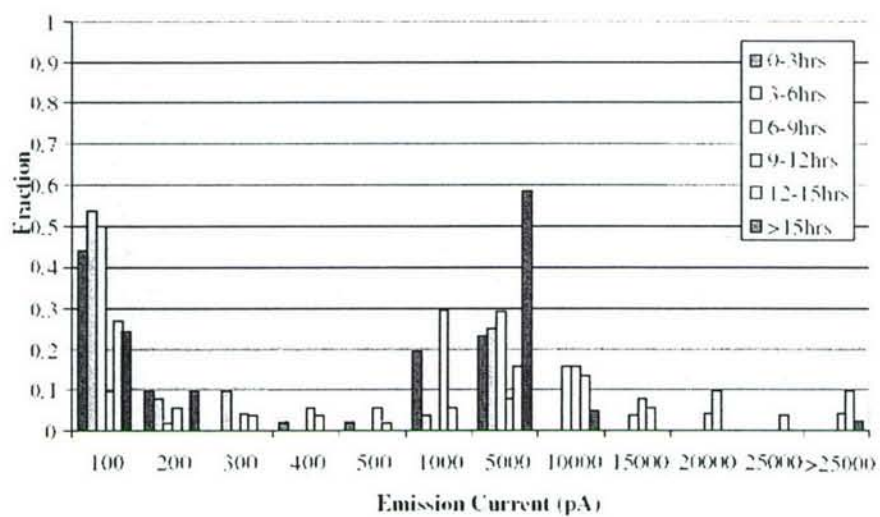


**Figure 3. Emission current histograms for readings at 12V bias in the voltage ramp cycles at different insulator thicknesses- a. 20 nm, and b. 25 nm.**





d.

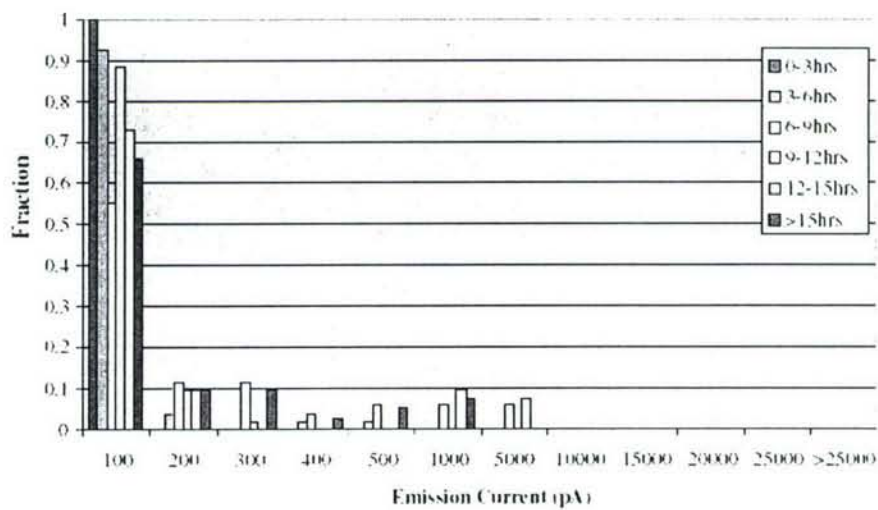


**Figure 3. Emission current histograms for readings at 12V bias in the voltage ramp cycles at different insulator thicknesses- c. 30 nm, and d. 40 nm.**

shows that a larger fraction of readings with emission current less than 100 pA is observed for the 30 nm than the 25 nm insulator thickness. The performance of the cold cathode emission after 10 hours of testing for the different insulator thicknesses is summarized in table 2, and indicates the fractions for readings recorded below 500 pA and for readings recorded above 1000 pA. The data suggests that the optimal insulator layer thickness is 25 nm considering both magnitude and longevity of emission current. The observation that the optimal device performance is at an intermediate insulator layer thickness is consistent with the expected performance at the extremes of the thickness range for the insulator. At smaller thicknesses the advantage of higher charge injection due to strong fields across the insulator is offset by an accelerated breakdown of the insulator, while at larger insulator thickness the longevity of the emission current is offset by lower cold cathode emission.

**Table 2**  
**Performance of cold cathode emission after 10 hours of testing - variation of insulator thickness**

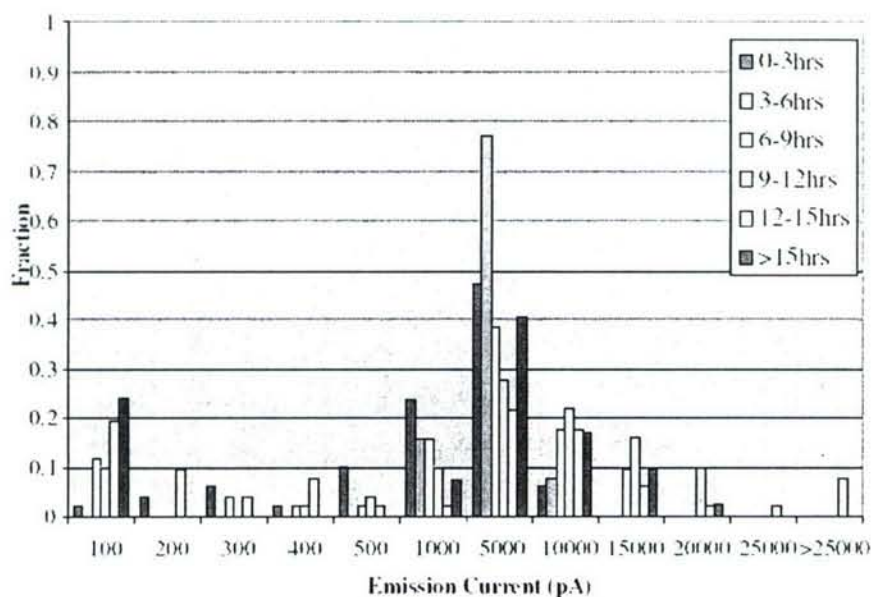
Thickness (nm)	Total fraction below 500 pA	Total fraction above 1000 pA
20	0.44	0.52
25 (#1)	0.26	0.70
25 (#2)	0.34	0.64
30	0.32	0.57
40	0.91	0.03

### 3.1.3. Variation of pressure of 20% Oxygen/Argon pressure for reactive evaporation of the insulator ( $\text{SiO}_x$ )

Reactive evaporation of  $\text{SiO}_2$  insulator layer results in non-stoichiometric films. The stoichiometry of the oxide insulator layer will determine the quality of the insulating layer in the device and have an effect on the performance of the cold cathode. The  $\text{SiO}_2$  layer was reactively evaporated in a 20% Oxygen/Argon environment at two background pressures of  $1 \times 10^{-6}$  Torr and  $8 \times 10^{-6}$  Torr. In both experiments, the thicknesses of the  $\text{SiO}_2$  insulator layer and the top Gold electrode were 25 nm. The results for reactive evaporation of insulator layer at  $1 \times 10^{-6}$  Torr in a background of 20% Oxygen/Argon mixture have been presented in the earlier sections. Figure 4 shows the histograms for reactive evaporation of  $\text{SiO}_2$  at the two Oxygen/Argon pressures. Emission current readings are recorded in the 1000-5000 pA range even in the early time bins for experiment at  $1 \times 10^{-6}$  Torr compared to that at  $8 \times 10^{-6}$  Torr, and the highest observed fraction in the same range reaches above 70% for the 3-6 hours time bin. The device performance, in terms of magnitude of the emission current, for the experiment at  $8 \times 10^{-6}$  Torr improves after test duration greater than 15 hours. A comparison the histograms for experiments at the two pressures after 15 hours of testing shows that devices in the  $8 \times 10^{-6}$  Torr experiment outperform devices in the  $1 \times 10^{-6}$  Torr experiment with regard to the



a.



b.

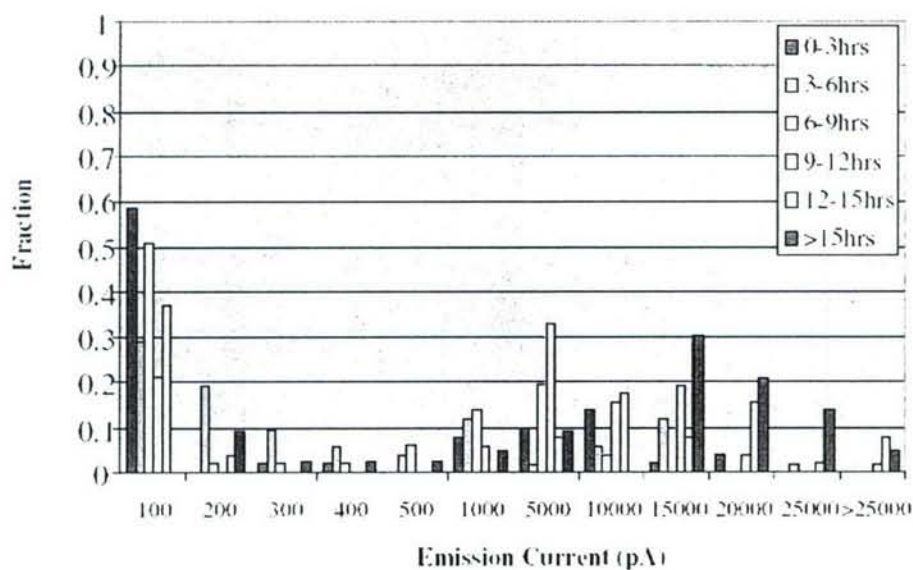


**Figure 4. Emission current histograms for readings at 12V bias in the voltage ramp cycles for reactive evaporation of  $\text{SiO}_2$  at different background pressures of 20% Oxygen/Argon mixture- a.  $1 \times 10^{-6}$  Torr, and b.  $8 \times 10^{-6}$  Torr.**

magnitude of the emission current. The cold cathode emission performance of the devices fabricated in the two experiments, each experiment carried out at either  $1 \times 10^{-6}$  Torr or  $8 \times 10^{-6}$  Torr 20% Oxygen/ Argon environment for reactive evaporation of the  $\text{SiO}_2$  layer, is presented in table 3. After 10 hours of testing, the fraction of emission current readings above 1000 pA is similar for devices fabricated in the two experiments. Since evaporating in a higher background pressure of the oxygen mixture results in shorter time to failure for the electron gun filament of the evaporator, the  $\text{SiO}_2$  insulator layer was reactively evaporated at  $1 \times 10^{-6}$  Torr in a background pressure of 20% Oxygen/Argon for all subsequent experiments.

**Table 3**  
**Performance of cold cathode emission after 10 hours of testing - variation of background pressure of 20% Oxygen/Argon for reactive evaporation of  $\text{SiO}_2$  layer**

Pressure (Torr)	Total fraction below 500 pA	Total fraction above 1000 pA
$1 \times 10^{-6}$ (#1)	0.26	0.70
$1 \times 10^{-6}$ (#2)	0.34	0.64
$8 \times 10^{-6}$	0.30	0.70

### 3.2. Improvements in cold cathode performance and characterization scheme

The variation of the fabrication parameters for  $\text{Ti/SiO}_x/\text{Au}$  devices, described in the previous sections, suggest that the fabrication procedure for optimal cold cathode performance consists of reactive evaporation of 250 Å  $\text{SiO}_2$  layer in an environment of 20% Oxygen/Argon at a pressure of  $1 \times 10^{-6}$  Torr, followed by deposition of 250 Å thick layer of Gold as the top metal electrode. The composition of the interface is expected to influence the magnitude of charge injected at the metal/insulator interface. Experiments were carried out to test the role of interface on charge injection, and it was found that devices composed of  $\text{Ti/Au/SiO}_x/\text{Au}$  devices emitted at higher currents than  $\text{Ti/SiO}_x/\text{Au}$  devices. All subsequent characterization of cold cathode performance was done for  $\text{Ti/Au/SiO}_x/\text{Au}$  devices since they showed enhanced emission current.

In addition to recording the total emission current at a series of voltage biases applied across the metal electrodes of the device, both the electron energy distributions and the device currents were measured as a function of the voltage bias. Two improvements in experimental design for device fabrication provided accurate measurements of energy distributions and device currents. Instead of fabricating a maximum of 24 devices on each glass substrate, only 12 devices were fabricated and tested in each experiment. The reduced density of fabricated devices on the glass substrate mitigated the effects of electric field imposed due to voltages on the metal electrodes, especially the top metal electrode, in the vicinity of the device under test.



This scheme, of fabricating only 12 devices on the glass substrate, also helped in implementing an improvement in accuracy of device current measurements. Figure 5 shows an array of 12 devices.

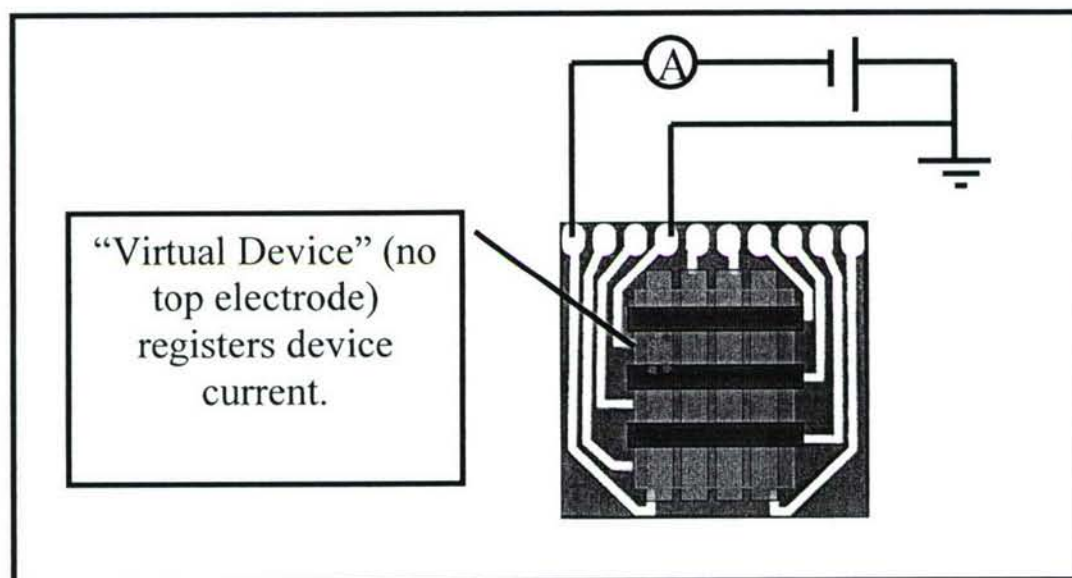


**Figure 5. Diagram depicting application of voltage bias across a pair of pre-patterned Gold electrodes, where the top metal electrode for device is absent.**

As shown in fig. 5, non-zero devices currents were measured when voltage bias was applied between a pair of pre-patterned Gold electrodes across a "virtual device", i.e., where a top electrode does not exist. The source of this error was due to thinning of the deposited layers at the edges of the mask as illustrated in fig. 6, and was confirmed by depositing sequential layers of the device in a displaced fashion (also shown in fig. 6).

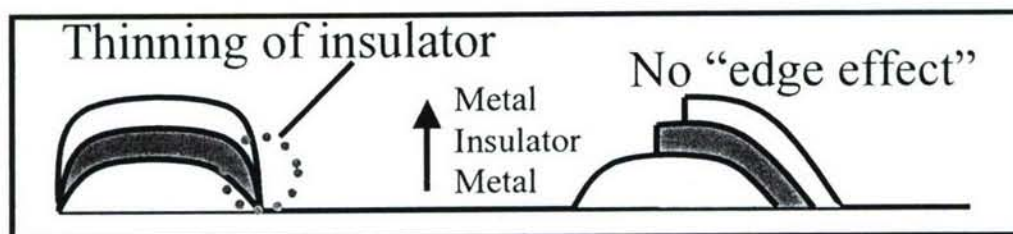


**Figure 6. Fabrication of MIM device to avoid thinning of device layers at the edges**

No device currents were recorded for “virtual devices” in the control experiment since electrical breakdown initiated by bias applied across thinned layers of the device was eliminated. Since the initial combinatorial screening experiments had already identified the optimal layer thicknesses and composition for best cold cathode performance, a simple mask, that patterns only 3 devices on the glass substrate and eliminates thinning of the layers at the edges of the active device area, was employed for experiments described in the subsequent sections.

### **3.3. Characterization of cold cathode performance for Ti/Au/SiO<sub>x</sub>/Au devices**

The electrical characterization of Ti/Au/SiO<sub>x</sub>/Au devices is described in the following sections. In all the experiments described in the subsequent sections, the optimal device fabrication parameters described in an earlier section were used. Devices were fabricated with an insulator thickness of 250 Å SiO<sub>x</sub> deposited by reactive evaporation at  $1 \times 10^{-6}$  Torr in a background pressure of 20% Oxygen/Argon, and 250 Å of Gold was deposited as the top metal electrode. The characterization of cold cathode performance consisted of device current measurements as a function of voltage bias, longevity of emission current, and electron energy distributions at a series of voltage biases.

#### **3.3.1. Voltage ramp cycles for device current measurement- Ti/Au/SiO<sub>x</sub>/Au**

When a voltage bias is applied across the MIM device, a device current is established between the metal electrodes. The device current measurements were made by applying voltage ramp cycles between 4-14V to the biased device. Interestingly, differences in I-V curves were observed even in back to back voltage ramp cycles. Some I-V curves, typically the early voltage ramp cycles, displayed negative differential resistance, i.e., device current decreased with increasing voltage bias. More reproducible I-V curves were observed in the later ramp cycles. The I-V curves showed a hysteresis when comparing I-V data for increasing voltage biases from 4V to 14V versus decreasing biases from 14V to 4V in the ramp cycle. Figure 7 shows an example for the I-V curves where the biased MIM device was cycled through 5 consecutive voltage ramp cycles spanning 4-14V.

Prior to these voltage ramp cycles, the device had undergone several similar rounds of testing, and the voltage bias was turned off after these tests. The device current at each voltage step is an average of acquisition over 10 s. In the first voltage ramp cycle, onset of negative differential resistance is observed at 10V and the I-V curve in the decreasing voltage ramp from 14V to 4V traces a different curve than the increasing voltage ramp from 4V to 14V. Subsequent to the first voltage ramp cycle, the I-V curves are very similar and display hysteresis for increasing versus decreasing voltage biases in the ramp cycle. The hysteresis in voltage ramp cycles suggests trapped charge in the insulator. Further, the observed negative differential resistance might be due to filling of trap states in the insulator. These hypotheses are consistent with the expectation that reactive evaporation of silicon dioxide results in non-stoichiometric oxide films.



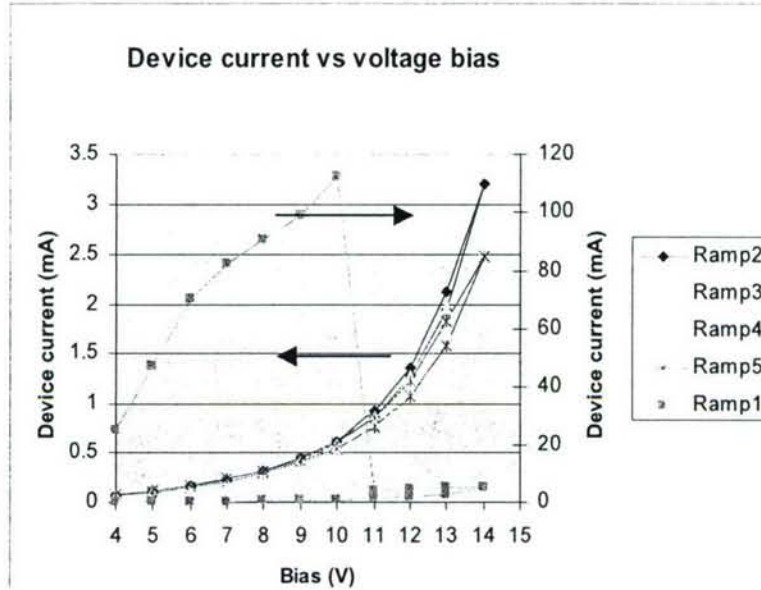


**Figure 7. Device current versus voltage bias for 5 consecutive voltage ramp cycles**

The observed device current in the voltage ramp cycles should be linked to the mechanism for electron transport across the insulator in the MIM device. As a first attempt to suggest a transport mechanism, the device current data presented in fig. 7 were fit to two mechanisms- Poole Frenkel and Schottky. The Poole-Frenkel mechanism is a bulk limited mechanism where carriers are injected into the conduction band of the insulator from trap states in the insulator by field-assisted lowering of the energy barrier. On the other hand, the Schottky mechanism is an interface limited mechanism where the electrons are injected from the Fermi level of the metal electrode into the conduction band of the insulator via thermal excitation. Figure 8 shows the Poole-Frenkel and Schottky plots for the fifth voltage ramp cycle presented in fig. 7. From the Schottky and Poole Frenkel plots, presented in fig. 8, the dielectric constant for the insulator can be estimated. The predicted dielectric constant by the Poole-Frenkel plot is 218.4, while the dielectric constant predicted by the Schottky plot is 24.2. These values are over estimated since, depending on the stoichiometry of the deposited insulator silicon dioxide, the expected value for the dielectric constant is in the range from  $\sim 4$  ( $\text{SiO}_2$ ) to  $\sim 6$  ( $\text{SiO}$ ). The prediction of higher dielectric constant might be due to several factors. If the insulator thickness has large variations across the device, then fixing the insulator thickness to a value predicted by the quartz crystal monitor might not be a good approximation. Alternatively, the higher apparent dielectric constant might suggest trapped charge in the oxide.



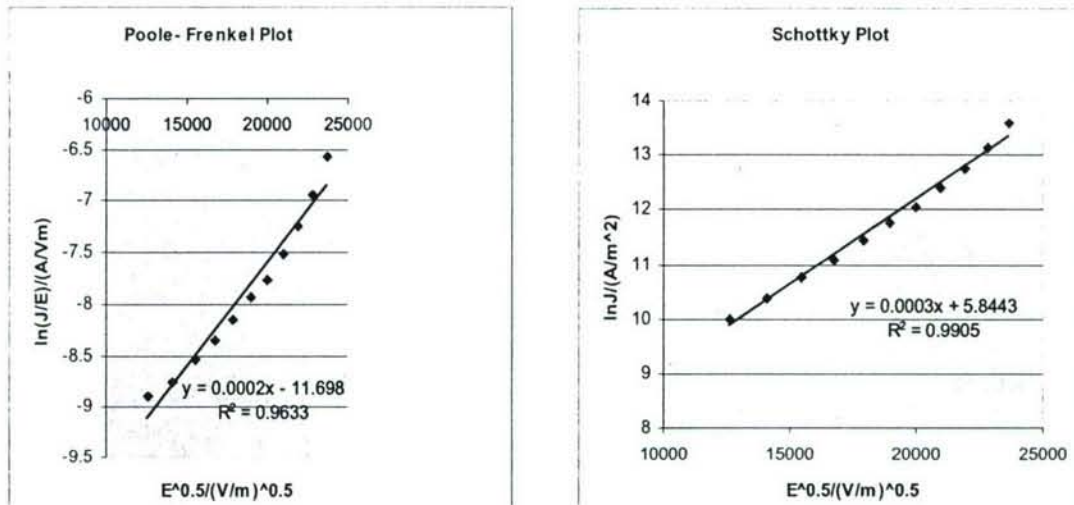


**Figure 8. Poole-Frenkel and Schottky plots for device current**

Several other transport mechanisms exist in the literature. For instance, the Fowler-Nordheim mechanism describes the transport by direct tunneling from the Fermi level of the injection metal electrode to the conduction band of the insulator. A Fowler-Nordheim plot shown in fig. 9, for the data discussed in fig. 8, indicated change in the slope at different field strengths applied across the insulator. This might indicate contributions of multiple transport mechanisms, and also possible differences in transport in low versus high field regimes.

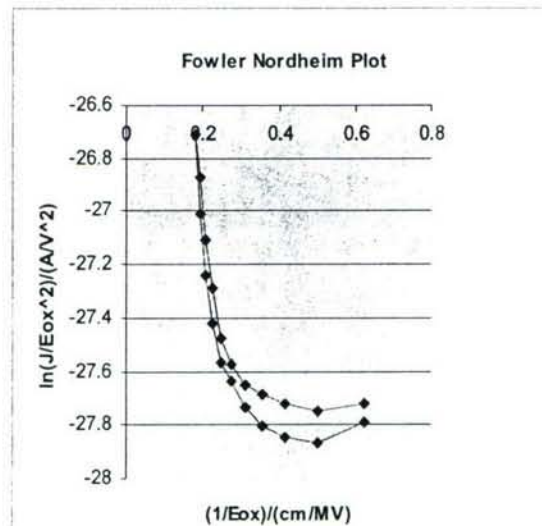


**Figure 9. Fowler-Nordheim plot for device current**

### 3.3.2. Effect of temperature on device current- Ti/Au/SiO<sub>x</sub>/Au

In a separate experiment, the I-V curves for the device current were recorded at a series of different device temperatures. The substrate, on which the MIM devices are fabricated, is in contact with a button heater. The substrate with fabricated devices was heated for 30 minutes and the voltage bias across the MIM device under test was turned on. The test consisted of 5 voltage ramp cycles to record the device current versus voltage bias. After the completion of the voltage ramp cycles, the voltage bias across the MIM device was turned off and the substrate was heated to a higher temperature for 30 minutes, followed by device current measurements. In each case, the voltage bias across the device was turned on only during acquisition of the device current data. The data for the last voltage ramp cycle was compared at different temperatures. Figure 10 shows the I-V device current data plotted as Schottky and Poole-Frenkel plots at different temperatures.

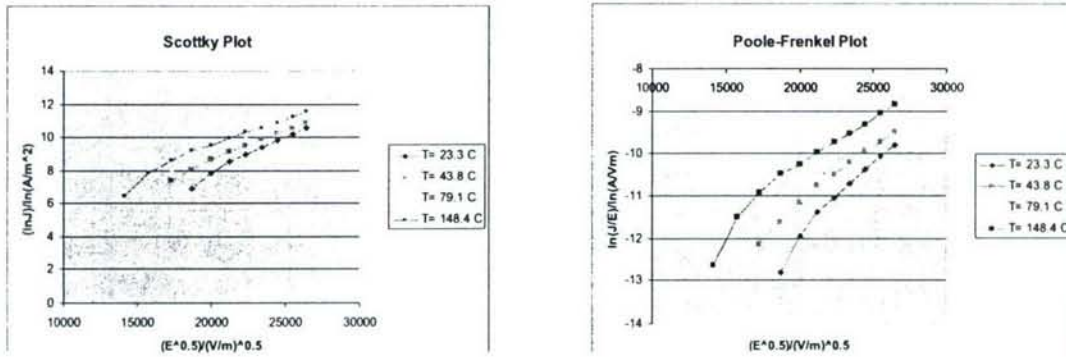


Figure 10. Schottky and Poole-Frenkel plots at different substrate temperatures

For both Schottky and Poole-Frenkel plots, the slope for the room temperature data is different compared to slope for the data at higher temperatures. Also, at a given temperature, the slope changes when comparing data for low versus high field regime. The change in slope in these plots again suggests contribution of multiple transport mechanisms.

### 3.3.3. Electron energy distributions- Ti/Au/SiO<sub>x</sub>/Au

In experiments reported in previous progress reports, electron energy distributions for Ti/SiO<sub>x</sub>/Au were presented. The electrical performance of the devices was characterized both, as a function of thickness of the insulator and the top metal electrode, and as a function of the background pressure of the chamber during reactive evaporation of silicon dioxide in a reactive atmosphere of Oxygen/Argon mixture. Devices that were fabricated in a background chamber pressure of  $1 \times 10^{-6}$  Torr of 20% Oxygen/Argon

mixture during reactive evaporation of silicon dioxide, combined with thickness parameters of 250 Å for the insulator and 250 Å for the top metal electrode, performed optimally in terms of total emission current and reliability of fabrication. In the current experiments, it was found that the emission from Ti/Au/SiO<sub>x</sub>/Au devices was higher than that from Ti/SiO<sub>x</sub>/Au devices. Electron energy distributions were acquired by varying the insulator thickness. The mean energy for the exoelectrons energy distributions for devices with different insulator thicknesses as a function of the applied voltage bias across the metal electrodes is shown in fig. 11.

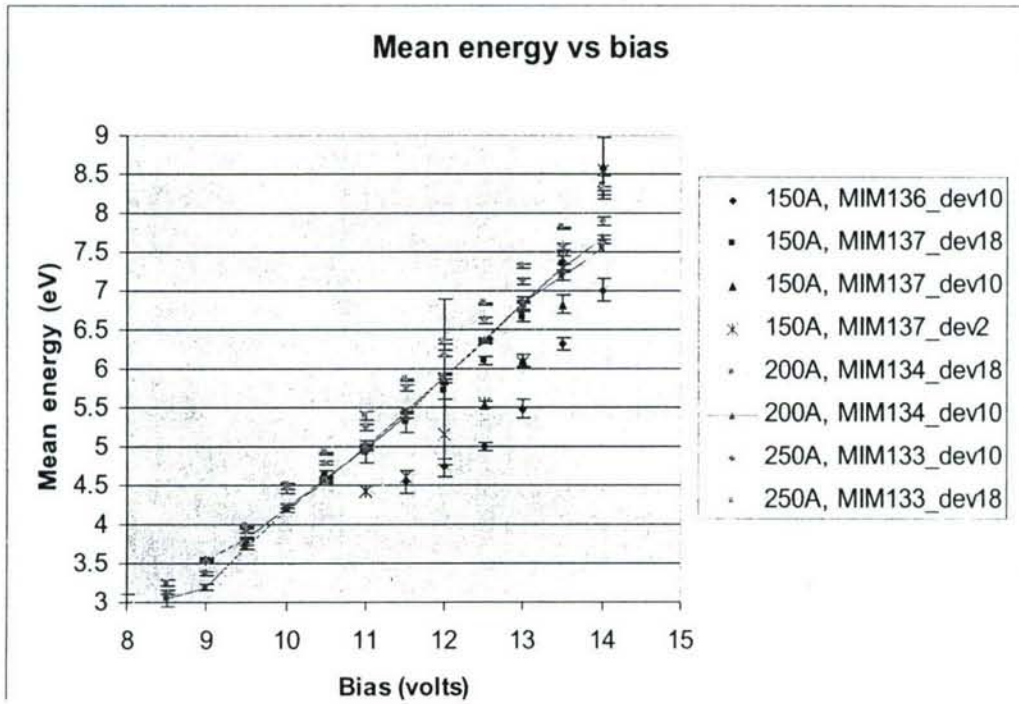


**Figure 11. Mean electron energy of the distribution versus voltage bias for different insulator thicknesses.**

The mean energy for the exoelectron energy distributions increases with increasing voltage bias, and the mean energy of the emission distribution from the MIM device is higher for an insulator thickness of 250 Å compared to 150 Å. A similar trend was observed for the Ti/SiO<sub>x</sub>/Au devices. Figure 11 illustrates larger variations in mean energy at a given voltage bias for devices with insulator thickness of 150 Å compared to devices with an insulator thickness of 250 Å. Considering the reproducibility of the mean energy trend for devices with insulator thickness of 250 Å, subsequent tests were performed on devices fabricated with 250 Å silicon dioxide insulator thickness.



### 3.3.4. Relaxation effects in device and emission currents- Ti/Au/SiO<sub>x</sub>/Au

The studies on Ti/SiO<sub>x</sub>/Au MIM devices were done by patterning 12 devices on the glass substrate. When a forward voltage bias is applied across the metal electrodes of the MIM device under test to observe vacuum emission, the other devices in the array are either reverse biased, not biased (i.e., no potential difference between the metal electrodes) or forward biased at less than 5V. This arrangement ensures that only emission from the forward biased MIM device is observed. However, it was found that the magnitude of total emission seemed to depend on the bias history of the device, and enhanced emission was found in many instances after applying other bias polarities before returning to a forward bias test. In the current set of experiments, only 3 devices are fabricated and all the devices share a common bottom electrode, while each device has a separate top electrode. A voltage bias was applied to only one device at a time, and the bias was alternated between forward bias, where vacuum emission is possible, and reverse bias, where electron emission will not be observed. Figure 12 shows both the device and emission currents as a function of time at a voltage bias of 12 V applied between the metal electrodes of the device. Every 60 minutes the voltage bias is alternated between forward and reverse bias. The forward bias data for device and emission currents that follow after a reverse bias period show enhanced emission. Both the device and emission currents relax to lower values compared to initial values during the forward bias tests. A related study of MIM devices for flat panel display applications observed increased longevity of emission and reduced degradation of the devices when reverse bias pulses were applied during tests for vacuum emission.<sup>3</sup> The reduction of charge accumulation in the insulator was suggested to play a role in the increased longevity of the devices.

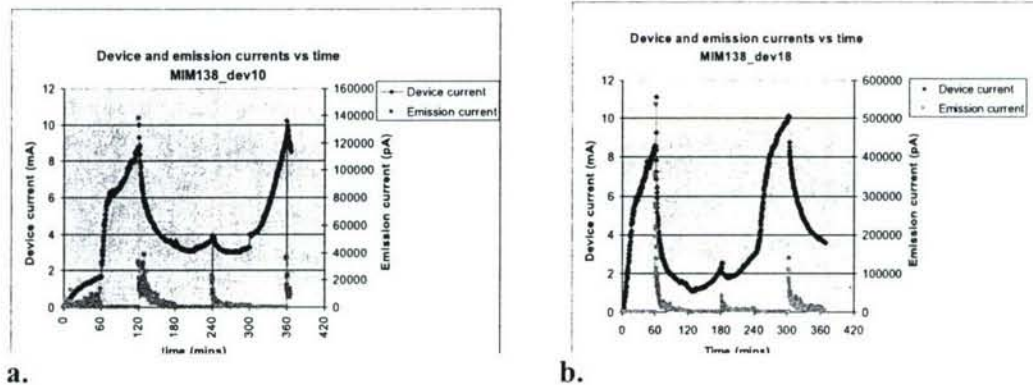


Figure 12. Device and emission currents versus time for alternating voltage biases- a. starting with forward bias, and b. starting with reverse bias

### 3.3.5. Lifetime test for emission current- Ti/Au/SiO<sub>x</sub>/Au

Another set of experiments were performed to evaluate longevity of electron emission when a constant voltage bias was applied between the metal electrodes of the MIM for extended periods of time. As described earlier, three MIM devices were fabricated on the glass substrate. Each device had no voltage bias history prior to the test. A constant voltage bias of 12 V was applied for typically 90 minutes, and the forward bias periods were alternated with periods of 15-60 minutes of no bias where the voltage bias applied across the MIM device was turned off. The application of constant forward bias alternated with no bias will provide information on how the MIM devices perform in terms of electron emission over extended periods of testing. Also, the yield as a function of time was determined from the tests by taking the ratio of the emission current to the device current. The forward biased device under test was positioned over the entrance to the hemispherical energy analyzer. The emission current was collected at the first ion-optic of the einzel lens at the entrance of energy analyzer assembly, and the first ion-optic of the einzel lens was connected to ground through a Keithley electrometer. This setup allowed for the simultaneous acquisition of electron energy distributions during the tests. Figure 13 shows the emission current and yield as a function of time for the tested devices. The MIM devices biased at constant voltage bias displayed sustained emission currents over long periods. The yield, defined as the ratio of emission current to device current, is between  $10^{-5}$  and  $10^{-6}$ , and is initially high. The emission current collected by a parallel plate assembly biased at 50V that collects all the emitted electrons was compared to the collection efficiency at the first ion-optic of the einzel lens. It was found that the collection efficiency at the einzel lens was between 25-50%. Hence, the actual yield could be higher by a factor of 2-4. Each device has an area of  $\sim 4 \text{ mm}^2$ . Considering the best performing device in this experiment ( $\sim 10 \text{ nA}$  emission current) at a constant voltage bias of 12V and the area of the device ( $\sim 4 \text{ mm}^2$ ), the emission current density is calculated to be  $2.5 \text{ mA/m}^2$ .

### 3.3.6. Emission current-Normalized energy distributions at series of voltage biases-Ti/Au/SiO<sub>x</sub>/Au

The shape of the energy distributions will be sensitive to the fluctuations in the emission current. A normalization of the raw counts in the energy scan by the emission current acquired during the scan will correct for the distortions in the shape due to fluctuations in emission current. Figure 14a shows the emission current normalized energy distributions at a series of voltage biases. Each scan is an average of 5 emission-current normalized scans and shows the broadening of the energy distributions at higher applied bias. Also, the peak of the energy distributions is tunable as a function of the voltage bias and is shown in fig. 14b. The area of the normalized scan increases with applied voltage bias between the metal electrodes of the MIM device. This might be explained by the energy dependent transmission efficiency of the hemispherical energy analyzer.



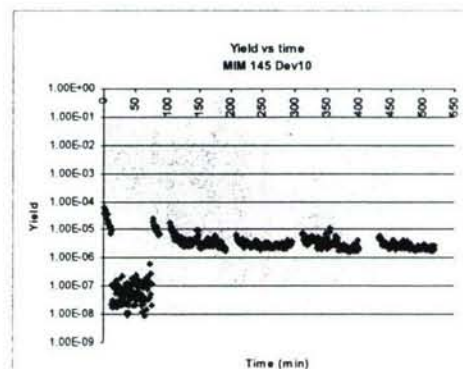
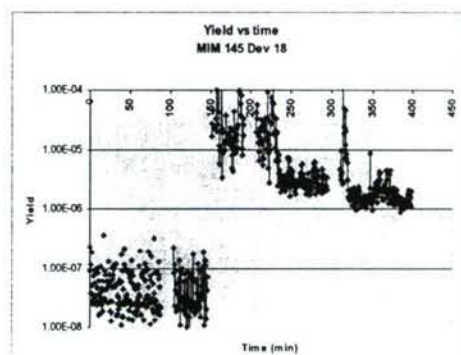
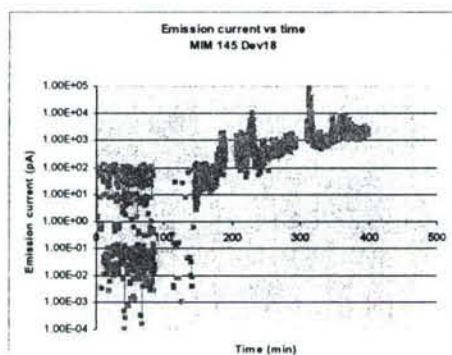
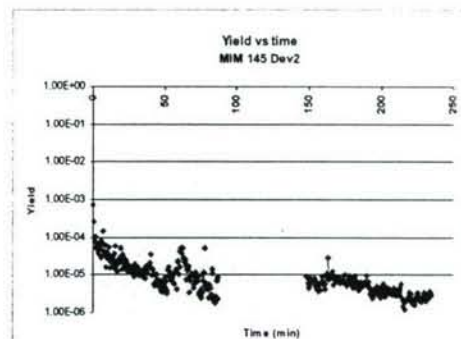
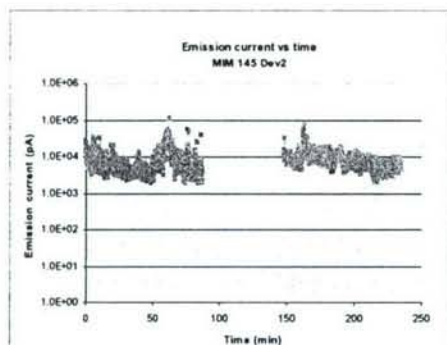
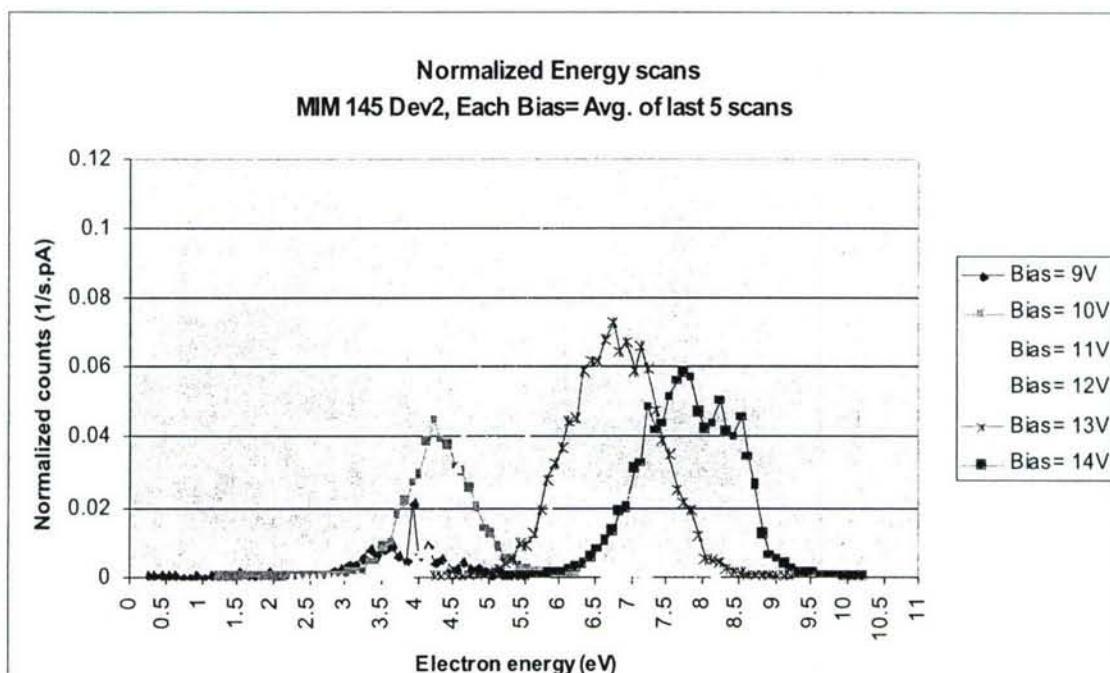
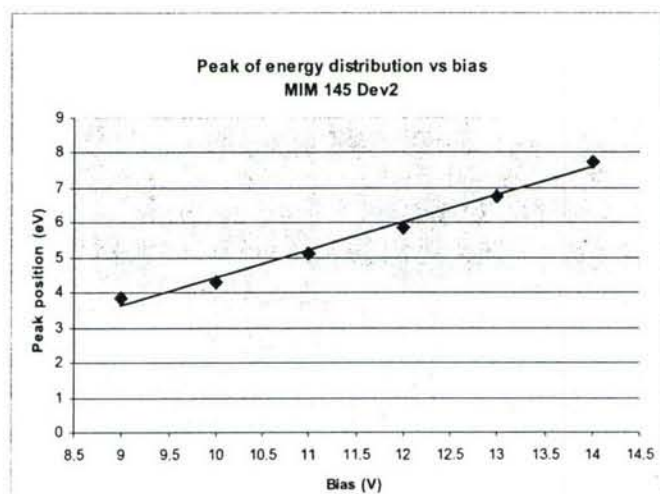


Figure 13. Emission current and yield versus time at constant applied voltage bias of 12V





**Figure 14a.** Emission-current normalized energy distributions at a series of voltage biases



**Figure 14b.** Peak energy of the distribution at different applied voltage biases between the metal electrodes of the MIM device

### 3.3.7. Transmission efficiency of hemispherical energy analyzer- Ti/Au/SiO<sub>x</sub>/Au

The hemispherical energy analyzer has an energy dependent transmission function that attenuates the transmission of low energy electron. In the experiments discussed in the previous sections, the top metal electrode was held at a constant voltage of -4.8 V, while a voltage bias, ranging from 4 V to 14 V, was applied between the top and the bottom metal electrodes of the MIM device. Since the top metal electrode is held at a constant voltage of -4.8 V, electrons emitted from the forward biased MIM device with a kinetic energy of 0 eV will gain an additional 4.8 eV energy when accelerated to the first ion-optic element of the einzel lens held at ground potential. In the current experiment, the transmission efficiency of the detector was determined empirically by generating vacuum electron emission from a forward biased MIM device. A constant voltage bias of 12 V was applied between the top and the bottom metal electrodes of the MIM device, and a series of energy distributions were acquired at different voltages at the top metal electrode of the MIM device. Since the voltage applied between the metal electrodes is constant, in principle, the same distribution in each case will be displaced along the energy axis depending on the additional energy imparted by the acceleration field between the top metal electrode and the first ion-optic element of the entrance einzel lens. The distributions acquired at different voltages on the top metal electrode were repeated in an interspersed manner to eliminate any systematic drifts. The value of the emission current-normalized counts at the peak in the energy distribution was plotted against the peak energy of the distribution. This represents the empirically determined transmission function for the hemispherical energy analyzer. A function of the form,  $A \cdot (1 - e^{-B(x-C)})$ , was fit to the empirical data. Figure 15 shows both the empirical data and the best fit for the transmission function.

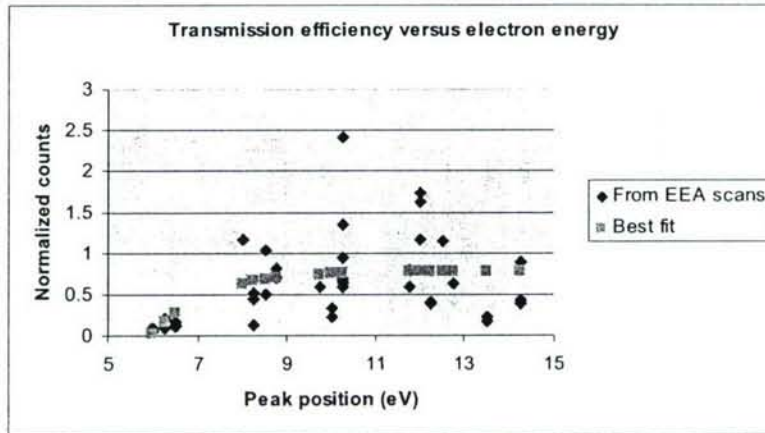


Figure 15. Empirically determined transmission function for the hemispherical energy analyzer



The data points for the transmission function show larger variations in normalized peak counts at higher electron energies. Nonetheless, the data clearly demonstrates a strong attenuation of low energy electrons. Also, the best fit curve for transmission efficiency traces the trend of strong attenuation at low electron energies and constant transmission efficiency at high electron energies. The previous experiments were done with a constant voltage of -4.8 V applied to the top electrode. Based on the empirically derived transmission efficiency, electrons emitted from the MIM at low energies in the range 0-1 eV will be filtered out of the detection when the top electrode is -4.8 V. Although applying a constant voltage in the range 10-15 V on the top electrode would ensure a constant transmission efficiency regime, the range of electron energies that can be scanned by the detector is limited due to the current circuit design for applying the voltages to the metal electrodes of the MIM device. In order to detect the low energy electrons, electron energy distributions were acquired at a series of voltage biases applied across the metal electrodes of the device by applying a constant voltage of -6.5 V to the top metal electrode. The results are presented in the next section and the electron energy distributions were corrected for the transmission efficiency.

### **3.3.8. Transmission corrected normalized distributions- Ti/Au/SiO<sub>x</sub>/Au**

Electron energy distributions, normalized to the emission current during the scans, were acquired at a series of voltage biases applied across the metal electrodes of the MIM device. The energy distributions were corrected for the transmission efficiency of the detector. Figure 16a shows the energy distributions at different voltage biases applied between the metal electrodes of the device. The electron energy distribution at each voltage bias in fig. 16a is an average of multiple energy scans, where each scan is normalized to the emission current and corrected for the transmission efficiency of the energy analyzer. The area of the energy distribution (for data presented in fig. 16a) versus applied voltage bias is shown in fig. 16b. The area of the normalized scan increases as a function of the applied voltage bias, and decreases for energy distributions recorded at the highest voltage biases of 13 V and 14V. The scans have already been corrected for energy dependent transmission efficiency of the energy analyzer. One possible explanation for the trend observed in fig. 16b might be due to differences in both, the collection efficiency at the first ion-optic element of the einzel lens for the low versus high energy electrons, and energy-dependent variation of the fraction of electrons admitted into the einzel lens entrance of the detector relative to the fraction of electrons collected at the first ion-optic element of the einzel lens.



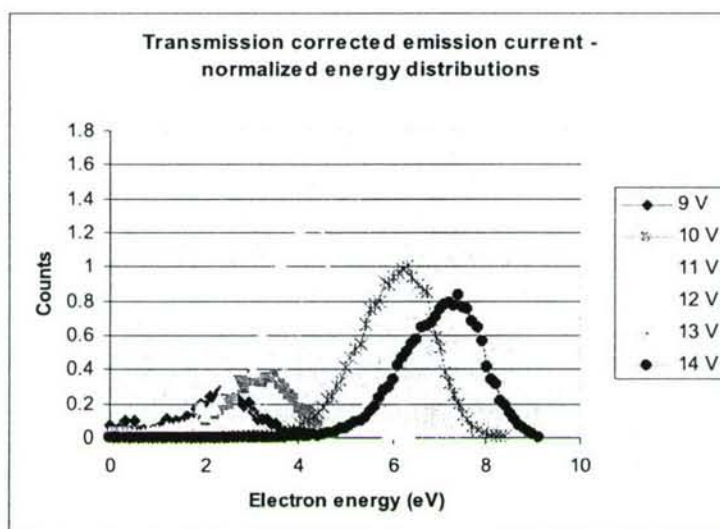


**Figure 16a.** Electron energy distributions versus voltage bias. Each energy distribution is normalized to the emission current and corrected for transmission efficiency of the detector.

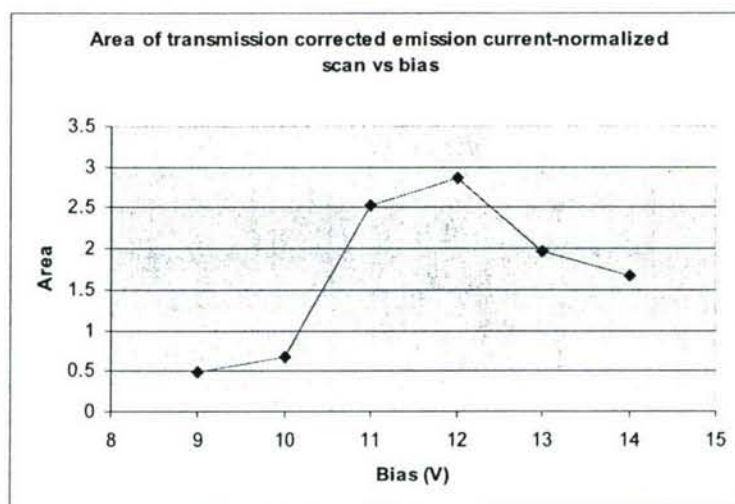


**Figure 16b.** Area of energy distribution versus voltage bias for distributions normalized to emission current and corrected for detector transmission efficiency.

### 3.4. Discussion

Early studies on MIM cold cathodes are summarized by Hrach in a review article.<sup>4</sup> When voltage bias above a threshold value is applied between the metal electrodes of the MIM device for some time, the device undergoes electroforming, which is a state of enhanced conductivity, and features including Voltage Controlled Negative Resistance (VCNR), vacuum electron emission, memory effects and switching are observed. One example where these effects are observed is the study by Khan et al. on Cu-SiO<sub>x</sub>-Cu devices.<sup>5</sup> The conduction mechanism and emission process has been explained by several theories.<sup>6-10</sup> The filamentary model<sup>8</sup> of Dearnaley et al., that is based on conduction by metallic filaments in the insulator, has been used by Sharpe and Palmer to model the electrical properties of Cu-SiO<sub>x</sub>-Cu devices.<sup>11</sup> In contrast to the filamentary conduction mechanism, Thurstans and Oxley have proposed that the forming process creates metallic islands in the insulator, and the electron transport in the device is mediated through activated tunneling mechanism between metallic islands.<sup>9</sup> Some groups have focused their study on vacuum emission and proposed mechanistic differences between emission occurring from formed versus non-formed sites in the MIM cold cathode.<sup>12,13</sup> In our study presented in this report, we have characterized the performance of Au-SiO<sub>x</sub>-Au cold cathodes. Some early studies on Au-SiO<sub>x</sub>-Au sandwich structures were carried out by Gould and Hogarth.<sup>14-15</sup> Gould and Hogarth electrically characterized the devices and suggested that a highly non-linear electric field in the insulator, resulting due to space charge in the insulator, determines the conduction mechanism. In our study of Au-SiO<sub>x</sub>-Au devices, in addition to recording the device current, we have studied the performance of cold cathode electron emission and acquired the energy distributions. The ensuing discussion draws on results for MIM sandwich structures presented in the literature and provides a qualitative interpretation of our experimental observations.

The conduction mechanism in MIM sandwich structures has been widely studied, and a survey of studies on MIM systems with oxide insulator<sup>10, 16-19</sup> should provide insights on understanding the electron transport mechanism in our study on Au-SiO<sub>x</sub>-Au MIM devices. In particular, studies on the M-SiO-M system<sup>16-18</sup> should be relevant since we employ reactive evaporation of SiO<sub>2</sub> in our studies that result in non-stoichiometric SiO<sub>x</sub> insulator layers in the MIM sandwiches. Hartman et al. studied conduction in Al-SiO-Al structures for SiO film thickness between 1000 and 10,000 Å.<sup>16</sup> An empirical equation for current density through SiO film was derived, and although the form of the empirical equation was similar to equations for Poole-Frenkel or Schottky conduction mechanisms, parameters like activation energy and dielectric constant derived by assuming either of the mechanisms were not in agreement with measured or reported values in the literature. They suggested that the current-voltage characteristics could be explained by O'Dwyer's theoretical study<sup>20</sup> that derives the conduction current assuming space charge buildup in the insulator film. Stuart studied the Al-SiO-Al system and explained the conduction mechanism by considering donors and trap states in the insulator.<sup>17</sup> Further evidence of interfacial space charge in M-SiO-M structure was provided through capacitance versus frequency measurements and SEM characterization by Roger et al.<sup>18</sup> The cross sectional SEM for the MIM sandwich at different applied



voltage biases demonstrated the existence of bias-dependent high field interfacial region in the SiO close to the positively biased metal electrode. In addition to the experimental studies described here, several theoretical studies have considered the role of trap states in the insulator and discussed the current-voltage characteristics for MIM structures.<sup>21-23</sup> In another study on a related system, the current noise in Al/Al<sub>2</sub>O<sub>3</sub>/Au sandwiches, with 17 nm thick Al<sub>2</sub>O<sub>3</sub> film in each MIM structure, was studied by Ošťádal et al.<sup>19</sup> The study revealed that the fluctuations of emission and leakage (conduction) current were not correlated, and an analysis of the fluctuations in leakage current indicated space charge fluctuations in the insulator as the noise source. The challenges in identifying the electron transport mechanism in MIM device is evident in the study by Sharpe and Palmer<sup>10</sup> who suggested different transport mechanisms in Cu-SiO<sub>x</sub>-Cu devices for low versus high field regime by trying curve fits for a large number of possible mechanisms. At voltages below 10V (insulator thickness between 300-500 Å), conduction either by a one dimensional Poole-Frenkel process or by tunneling between adjacent traps was suggested, while at voltages above 10 V an additional contribution due to Fowler-Nordheim tunneling directly into the conduction band of the insulator explained the observed experimental data. The electrical characterization of Au-SiO<sub>x</sub>-Au devices in our study demonstrates similar trends discussed so far, where fitting the data to either the electrode-limited Schottky mechanism or bulk-limited Poole-Frenkel mechanism did not yield the correct dielectric constant. Also, common with the studies discussed here, both the Schottky and Poole-Frenkel plots for our experimental data showed two linear regions with different slopes depending on the voltage regime, suggesting that multiple transport mechanisms influenced by the space charge in the insulator might be responsible for the conduction process.

The presence of trap states in the insulator layer of the MIM structure and its influence on the electrical properties has been discussed in the literature. Two studies<sup>24-25</sup> presented in the literature are particularly relevant in understanding our experimental observations. Suzuki et al. developed a scheme to characterize the quality of the tunneling insulator in MIM cold cathodes by I-V measurements at low electrical stress.<sup>24</sup> A pulsed low voltage bias was applied between the metal electrodes and the current was monitored as a function of time after the initial charging current to the MIM capacitor had diminished. A relaxation current proportional to inverse of the elapsed time was observed. This observed time dependence was ascribed to charge injection from the bottom electrode to unoccupied trap states,<sup>26-27</sup> and the constant of proportionality, related to the number of unoccupied trap states, was used to access the quality of the insulator. In a different study by Ramprasad,<sup>27</sup> simultaneous contributions from multiple transport mechanisms was modeled for metal-insulator-metal capacitor systems, and both J-t and J-V (J is the current density) characteristics were predicted. The phenomenological theory used parameters typical for TaO<sub>x</sub> capacitors and oxide thickness of several hundred angstroms. The model included trap-assisted tunneling, Schottky effect and a modified Poole-Frenkel mechanism that accounts for the time varying trapped electrons in the insulator. The short time behavior of the current density shows an inverse relation to time and is attributed to trap-assisted tunneling, while, at later time, the principal contribution is due to Schottky and modified Poole-Frenkel effects. These studies are relevant to interpreting experimental data on Au-SiO<sub>x</sub>-Au



devices presented in this report. At a constant voltage bias applied between the metal electrodes of the MIM device, relaxation in device current was observed with time as shown in fig. 12. In many instances, the relaxation observed in the emission current could be scaled by constants to resemble the relaxation in the device current. Interestingly, alternating the voltage bias between forward and reverse voltage biases increased the magnitudes of the device and emission currents before the currents relaxed again. The increase in the magnitude of the currents following test with reverse voltage bias might be due to emptying of the trap states in the insulator. This explanation has been suggested in some studies.<sup>3,24</sup> Suzuki et al.<sup>3</sup> studied the effect of applying different reverse voltage pulses on the diode current monitored as a function of time, and suggested an optimized AC driving method for improving lifetime of the cathode. As discussed by Ramprasad,<sup>25</sup> the J-t behavior affects the J-V characteristics and depends on the measurement interval. One interesting feature in the diode current versus voltage bias plot is a Voltage Controlled Negative Resistance (VCNR), shown in fig. 7, and has been observed in other studies.<sup>5,15,28</sup> The studies of both, Gould and Hogarth<sup>15</sup>, and Khan and Hogarth,<sup>5</sup> explained VCNR based on the filamentary model, where VCNR occurs due to rupture of filaments at high voltage biases. Both studies reported disappearance of negative resistivity on repeated voltage traces at temperatures below a critical value. Sakemura et al. injected charge from a Si layer into SiO<sub>x</sub> layer and reported high electron emission efficiency for the electron emitter.<sup>28</sup> Similar to our observations in fig. 7, Sakemura et al. observed VCNR and hysteresis behavior in the device current characteristics, and VCNR disappeared in the subsequent voltage cycles. An alternative explanation to the filamentary model to explain VCNR could be the dynamics of filling and emptying of trap states. Chen et al.<sup>29</sup> have studied the influence of trapped charges on stress induced leakage current in SiO<sub>2</sub> thin films, and suggested that the negative differential resistance arises due to release of trapped electrons in the gate/oxide interface region during I-V measurement.

The filamentary model for conduction implies local paths of high conductivity that are responsible for the emission from cold cathodes. Sharpe and Palmer<sup>10</sup> estimated the emission area to be  $10^{-14}$  m<sup>2</sup> from the Fowler-Nordheim plots for their experimental data on Cu-SiO<sub>x</sub>-Cu devices. In the context of possible localized sites in cold cathode emission, it is worthwhile to discuss some studies reported in the literature,<sup>13, 30-31</sup> carried out at a microscopic level, that offer useful mechanistic insight. Ohtsuka et al. observed the emission from Al-AlO<sub>x</sub>-Pt electron emitters (50  $\mu$ m diameter) using a photoelectron emission microscope in a UHV chamber. The emission pattern consisted of sharp spots with diameter of  $\sim 3$   $\mu$ m. An analysis of the emission current intensity fluctuations for each individual spot revealed two different power spectra for the fluctuations, where one spectrum was related to high emission spots from formed sites, and the other spectrum was assigned to low emission spots from non-formed sites. The fluctuations in leakage current were also recorded. Since electron transport in the cold cathode occurs across the insulator layer separating the metal layers, the microscopic properties of the insulator should play a role in the observed fluctuations. The results presented in two different studies on SiO<sub>2</sub> carried out using microscopy offer additional mechanistic insights.<sup>30-31</sup> Ludeke and Wen<sup>30</sup> performed Ballistic Electron Emission Microscopy (BEEM) by injection of electrons from a STM tip into the metal gate of a MOS structure. The oxide



in the MOS structure was 71 Å thick thermally grown SiO<sub>2</sub> layer. The local potential experienced by the injected electrons is strongly affected by the trapped charge, and determination of the threshold voltage to observe a collector current helps in deducing the approximate location of the charge in the oxide. Spatial variations in the threshold voltage, as high as 2 eV, were observed on the nanometer scale and magnitude of the threshold voltage at a given spatial location depended on the history of electron beam exposure in the same area. In the same study, the trapped charge was modeled as a series of parallel charge sheets and the potential distribution in the oxide, that was consistent with the observed threshold voltages, was derived. The derived potential in the oxide was inhomogeneous as a function of the distance from the metal-oxide interface. Similar spatial variations in electrical properties at a microscopic level were revealed in a study by Pakes et al. where Conductive Atomic Force Microscopy (CAFM) was employed to image quasibreakdown sites in native SiO<sub>2</sub> films (~ 3 nm).<sup>31</sup> Local current-voltage spectroscopy was performed using contact mode AFM, and low biases were applied to avoid creation of additional traps and unravel the role of native traps in quasibreakdown fluctuations in the tunneling current. Enhanced local conductivity regions, on the order of 100 nm<sup>2</sup>, were observed. The model for the tunnel current included a conduction path between *n* identical tunnel junctions. The fluctuations in the tunnel current were attributed to charge-noise effects in trap states within the conduction path. Similar effects are expected in the Au-SiO<sub>x</sub>-Au devices studied in our experiments since the SiO<sub>x</sub> layer, owing to its non-stoichiometry, has a high trap density.

Several studies on optimization of cold cathode performance have been reported in the literature.<sup>32-35</sup> Kusunoki increased the emission current from MIM cathode by using a multilayer Ir-Pt-Au as the top electrode.<sup>32</sup> The Ir layer ensured durability, Pt layer prevented intermixing, and Au layer was best suited due to the long mean free path. Since we employ electron beam evaporation, deposition of the same multilayer composition is not feasible. In our studies, we have screened for Ti/Au and Cr/Au, with Ti or Cr as the wetting layer on the insulator, and compared with the cold cathode performance for Au as the top electrode layer. The emission current, if observed in the former cases, was very small compared to emission current with Au as the top metal electrode. Although the interface between Au and SiO<sub>x</sub> is weak, we decided to use Au as the top metal electrode considering the superior emission and chemical inertness, a property that can facilitate future studies in hot electron initiated chemistry. The reason for the poor performance of Ti/Au and Cr/Au combination might at least partly be explained by the reactive nature of the interface. Govyadinov et al.<sup>35</sup> have screened several combinations of metals for the top electrode in a polysilicon MIS electron emitter and experimentally determined that porous metal film improved the emission efficiency of the MIS device compared to a device with dense continuous metal layer as the top electrode. In our studies of devices with Ti/Au or Cr/Au as the top metal electrode, the wetting layer will promote formation of a more uniform Au layer and thus, similar to the observation by Govyadinov et al., decrease the emission current. Improvement in the cold cathode performance was achieved by Kusunoki et al.<sup>33</sup> by optimizing the thickness of the insulator in MIM electron emitters. The insulator layer was anodized Al<sub>2</sub>O<sub>3</sub> and the transfer ratio, defined as the ratio between the emission and device currents, was determined as a function of the insulator thickness. The transfer ratio was 0.7% at the



optimal insulator thickness. The observed dependence of transfer ratio on the insulator thickness was modeled by simulating the scattering process in the insulator and determining the electron energy distribution at the insulator-top metal electrode interface. This calculation provided a qualitative understanding and the predicted transfer ratio deviated from the experimentally observed values by an order of magnitude. The reason for the variation between predicted and observed transfer ratios was attributed both, to additional scattering losses in the top metal electrode not included in the model, and to approximations arising by considering a defect free insulator. The authors indicate that the energy losses due to trapping and detrapping of electrons in the insulator will have a significant contribution in insulators with high trap states. In our studies, the observed yield (transfer ratio), plotted in fig. 13, is between  $10^{-5}$ - $10^{-6}$ . The low yields in our studies compared to that reported by Kusunoki et al. might be due to significant energy losses due to trapping and detrapping processes in the  $\text{SiO}_x$  insulator layer. Nonetheless, we observed an emission current density on the order of  $1\text{mA/m}^2$ , a regime of the emission current density where useful aerospace applications or hot electron initiated chemistry is feasible.

In summary, the trap states in the non-stoichiometric  $\text{SiO}_x$  insulator in the Au- $\text{SiO}_x$ -Au devices play an important role in determining the conduction mechanism. The trap states facilitate transport either through trap-assisted tunneling, direct hopping between the trap states or contributing to a bulk-limited Poole-Frenkel effect. Multiple transport mechanisms contribute to the conduction current with differences for low versus high electric field transport. The energy distributions for the emitted electrons peak at quasiballistic energies. Similar emission at high energies was observed by Sakemura et al.<sup>28</sup> in their study on developing a high efficiency electro-emission device. A Si layer deposited on the bottom metal electrode was used to inject electrons in a  $\text{SiO}_x$  drift layer sandwiched between the two metal electrodes. The authors suggested a hopping mechanism for voltages below the threshold voltage for negative resistance. The appearance of negative resistance was attributed to electron trapping in the drift layer. Further, they proposed that a non-uniform electric field in the  $\text{SiO}_x$  layer, with enhanced field near the top electrode, mediates the transport of electrons in the device. We believe that a similar conduction mechanism occurs in the Au- $\text{SiO}_x$ -Au devices.

## 4. Summary

Cold cathode Metal-Insulator-Metal (MIM) devices were fabricated and tested. A combinatorial approach was used to screen for the optimal fabrication procedure and layer composition. The emission current density on the order of  $1\text{mA/m}^2$  was achieved, and sustained emission over long periods of testing was observed. The transfer ratio, i.e., the ratio between the emission and device currents, was between  $10^{-5}$ - $10^{-6}$ . A plausible transport mechanism that is consistent with our experimental data and other studies reported in the literature is discussed. The in-situ fabrication and testing of devices presented in this report makes it feasible to employ these devices in future studies on hot electron initiated chemistry as reported in some studies.<sup>36-37</sup>



## 5. References

1. G. I. Mishin, "Sonic and shock wave propagation in weakly ionized plasmas," *Gas Dynamics*, New York: Nova Science Publishers, pp. 81ff (1992).
2. A. A. Dixit, A. Raigoza, T. Engstrom, A. Lapicki, K. Akutsu, and D. C. Jacobs, "A solid-state approach to generating hot electrons", *American Institute of Aeronautics and Astronautics*, AIAA 2005-207: 1-7 (2005).
3. M. Suzuki, T. Kusonoki, M. Sagawa, and K. Tsuji, "Improvement of lifetime and emission current of metal-insulator-metal cathodes for field-emission displays", *International Display Research Conference*, pp. 390-393, (2000)
4. R. Hrach, "Electron emission from MIM systems and discontinuous metal films", *International Journal of Electronics*, **73**(5), pp. 841-847 (1992).
5. G. A. Khan and C. A. Hogarth, "Electroforming in MIM structures of  $\text{SiO}_x$  and  $\text{SiO}_x/\text{SnO}$  composite dielectric thin films", *Journal of Materials Science*, **27**, pp. 2613-2618 (1992).
6. T. W. Hickmott, "Potential distribution and negative resistance in thin oxide films", *Journal of Applied Physics*, **35**(9), pp. 2679-2689 (1964).
7. J. G. Simmons and R. R. Verderber, "Conduction and reversible memory phenomena in thin insulating films", *Proceedings of the Royal Society of London, Series A: Mathematical, Physical and Engineering Sciences*, **301**(1464), pp. 77-102 (1967).
8. G. Dearnaley, D. V. Morgan, and A. M. Stoneham, "A model for filament growth and switching in amorphous oxide films", *Journal of Non-Crystalline Solids*, **4**, pp. 593-612 (1970).
9. R. E. Thurstans and D. P. Oxley, "The electroformed Metal-Insulator-Metal structure: A comprehensive model", *Journal of Physics D: Applied Physics*, **35**, pp. 802-809 (2002).
10. R. G. Sharpe and R. E. Palmer, "Evidence for field emission in electroformed Metal-Insulator-Metal devices", *Thin Solid Films*, **288**, pp. 164-170 (1996).
11. R. G. Sharpe and R. E. Palmer, "Regeneration of electroformed Metal-Insulator-Metal devices: A new model", *Journal of Physics: Condensed Matter*, **8**, pp. 329-338 (1996).
12. T. Kusunoski, M. Suzuki, S. Sasaki, T. Yagushi, and T. Aida, "Fluctuation-free electron emission from non-formed Metal-Insulator-Metal (MIM) cathodes fabricated by low current anodic oxidation", *Japanese Journal of Applied Physics*, **32**, pp. L1695-L1697 (1993).

13. M. Ohtsuka, T. Kusaka, M. Yamanobe, and S. Kawate, "Emission microscope observation of Metal-Insulator-Metal emitters", *Japanese Journal of Applied Physics*, **42**, pp. 7525-7528 (2003).
14. R. D. Gould and C. A. Hogarth, "Current-voltage characteristics, dielectric breakdown and potential distribution measurements in Au-SiO<sub>x</sub>-Au thin film diodes and triodes", *International Journal of Electronics*, **37(2)**, pp. 157-175 (1974).
15. R. D. Gould and C. A. Hogarth, "Low temperature conduction and breakdown phenomena in Au-SiO<sub>x</sub>-Au thin-film sandwich structures", *International Journal of Electronics*, **38(5)**, pp. 577-591 (1975).
16. T. E. Hartman, J. C. Blair, and R. Bauer, "Electrical conduction through SiO films", *Journal of Applied Physics*, **37(6)**, pp. 2468-2474 (1966).
17. M. Stuart, "Conduction in silicon oxide films", *British Journal of Applied Physics*, **18**, pp. 1637-1640 (1967).
18. Jean-Alain Roger, C. H. S. Dupuy, and Stephen J. Fonash, "Evidence for interfacial space-charge regions in electron-beam-evaporated SiO", *Journal of Applied Physics*, **46(7)**, pp. 3102-3105 (1975).
19. I. Ošťádal, L. Lečko, and P. Sobotík, "Current noise in thin film Al/Al<sub>2</sub>O<sub>3</sub>/Au sandwiches", *Vacuum*, **50(1-2)**, pp. 9-13 (1998).
20. J. J. O'Dwyer, "Current-voltage characteristics of dielectric films", *Journal of Applied Physics*, **37(2)**, pp. 599-601 (1966).
21. D. V. Geppert, "Space-charge-limited tunnel emission into an insulating film", *Journal of Applied Physics*, **33(10)**, pp. 2993-2995 (1962).
22. J. G. Simmons and G. W. Taylor, "Dielectric relaxation and its effect on the isothermal electrical characteristics of defect insulators", *Physical Review B*, **6(12)**, pp. 4793-4803 (1972).
23. H. M. Gupta and R. J. Van Overstraeten, "Role of trap states in the insulator region for MIM characteristics", *Journal of Applied Physics*, **46(6)**, pp. 2675-2682 (1975).
24. M. Suzuki, M. Sagawa, T. Kusunoki, and K. Tsuji, "Characterization of the tunneling insulator in MIM cathodes by low-stress I-V measurement", *IEEE Transactions on Electron Devices*, **50(4)**, pp. 1125-1130 (2003).
25. R. Ramprasad, "Phenomenological theory to model leakage currents in metal-insulator-metal capacitor systems", *Phys. Stat. Sol. (b)*, **239(1)**, pp. 59-70 (2003).



26. T. R. Oldham, A. J. Lelis, and F. B. McLean, "Spatial dependence of trapped holes determined from tunneling analysis and measured analysis", *IEEE Trans. Nuclear Sci.*, **33**, pp. 1203-1209 (1986).
27. D. J. Dumin and J. R. Maddux, "Correlation of stress-induced leakage current in thin oxides with trap generation inside oxides", *IEEE Transactions on Electron Devices*, **40**, pp. 986-993 (1993).
28. K. Sakemura, N. Negishi, T. Yamada, H. Satoh, A. Watanabe, T. Yoshikawa, K. Ogasawara, and N. Koshida, "Development of an Advanced High Efficiency Electro-Emission Device", *Journal of Vacuum Science and Technology B*, **22(3)**, pp. 1367-1371 (2004).
29. T.P. Chen and Y. L. Luo, "Influence of trapped charges on low-level leakage current in thin silicon dioxide films", *IEEE Conference*, **2797**, pp. 974-977 (2001).
30. R. Ludeke and H. J. Wen, "Localized electron trapping and trap distributions in SiO<sub>2</sub> gate oxides", *Applied Physics Letters*, **71(21)**, pp. 3123-3125 (1997).
31. C. I. Pakes, S. Ramelow, S. Prawer, and D. N. Jamieson, "Nanoscale electrical characterization of trap-assisted quasibreakdown fluctuations in SiO<sub>2</sub>", *Applied Physics Letters*, **84(16)**, pp. 3142-3144 (2004).
32. T. Kusunoski and M. Suzuki, "Increasing Emission Current from MIM Cathodes by Using an Ir-Pt-Au Multilayer Top Electrode", *IEEE Transactions: Electronic Devices*, **47(8)**, pp. 1667-1672 (2000).
33. T. Kusunoski, M. Sagawa, M. Suzuki, A. Ishizaka, and K. Tsuji, "Emission Current Enhancement of MIM Cathodes by Optimizing the Tunneling Insulator Thickness", *IEEE Transactions on Electron Devices*, **49(6)**, pp. 1059-1065 (2002).
34. A. Baba, T. Yoshida, and T. Asano, "Field Emission Characteristics of Defect-Controlled Polyimide Tunneling Cathode", *Journal of Vacuum Science and Technology B*, **22(3)**, pp. 1353-1357 (2004).
35. A. Govyadinov, T. Novet, D. Pidwerbecki, S. Ramamoorthi, J. Smith, J. Chen, C. Otis, D. Neiman, and P. Benning, "Polysilicon metal-insulator-semiconductor electron emitter", *Journal of Vacuum Science and Technology B*, **23(2)**, pp. 853-863 (2005).
36. R. G. Sharpe and R. E. Palmer, "The Gas Sensitivity of Device and Emission Currents in an electroformed MIM device", *Journal of Physics: Applied Physics*, **29**, pp. 837-842 (1996).
37. R. G. Sharpe, St. J. Dixon-Warren, P. J. Durston, and R. E. Palmer, "The Electronic Catalyst: Dissociation of Chlorinated Hydrocarbons by Metal-Insulator-Metal Electron Emitters", *Chemical Physics Letters*, **234**, pp. 354-358 (1995).

## **6. Personnel Supported**

The following individuals have been supported by this grant:

Prof. Dennis C. Jacobs, Faculty

Dr. Amitavikram A. Dixit, Postdoctoral Research Associate

Annette Raigoza, Graduate Research Assistant

## **7. Publications**

A. F. Raigoza, "Metal-Insulator-Metal (MIM) Nanodevices", *Masters' Thesis*, University of Notre Dame (2006).

A. A. Dixit, A. Raigoza, T. Engstrom, A. Lapicki, K. Akutsu, and D. C. Jacobs, "A Solid-State Approach to Generating Hot Electrons", *American Institute of Aeronautics and Astronautics*, AIAA 2005-207: 1-7 (2005).

## **8. Interactions/Transitions**

The results of this project were presented at:

- 43<sup>rd</sup> AIAA Aerospace Sciences Meeting in January, 2005
- 230<sup>th</sup> ACS National Meeting in August, 2005
- 52<sup>nd</sup> AVS International Symposium in October, 2005

## **9. Inventions or Patent Disclosures**

None

## **10. Honors and Awards**

25<sup>th</sup> Donald G. Davis Memorial Lecture at the University of New Orleans

Distinguished Alumnus in the School of Physical Sciences, University of California at Irvine